Title

Multiscale electric-field imaging of polarization vortex structures in PbTiO3/SrTiO3 superlattices

Journal

APL Materials, 11(5)

ISSN

2166-532X

Authors

Addiego, Christopher

Zorn, Jacob A

Gao, Wenpei

et al.

Publication Date

2023-05-01

DOI

10.1063/5.0146713

APL Materials

RESEARCH ARTICLE | MAY 04 2023

Multiscale electric-field imaging of polarization vortex structures in $PbTiO_3/SrTiO_3$ superlattices

Christopher Addiego; Jacob A. Zorn; Wenpei Gao; ... et. al

APL Mater 11, 051106 (2023)
https://doi.org/10.1063/5.0146713

Multiscale electric-field imaging of polarization vortex structures in $PbTiO_3/SrTiO_3$ superlattices

Cite as: APL Mater. 11, 051106 (2023); doi: 10.1063/5.0146713
Submitted: 16 February 2023 • Accepted: 19 April 2023 •
Published Online: 4 May 2023

Christopher Addiego,[1] Jacob A. Zorn,[2] Wenpei Gao,[3] Sujit Das,[4] Jiaqi Guo,[1] Chengqing Qu,[1] Liming Zhao,[1] Lane W. Martin,[4,5] Ramamoorthy Ramesh,[4] Long-Qing Chen,[2] and Xiaoqing Pan[1,3,6,a)]

AFFILIATIONS

[1] Department of Physics and Astronomy, University of California, Irvine, California 92697, USA
[2] Department of Materials Science and Engineering and Materials Research Institute, The Pennsylvania State University, University Park, Pennsylvania 16802, USA
[3] Department of Materials Science and Engineering, University of California, Irvine, California 92697, USA
[4] Department of Materials Science and Engineering, University of California, Berkeley, California 94720, USA
[5] Materials Sciences Division, Lawrence Berkeley National Laboratory, Berkeley, California 94720, USA
[6] Irvine Materials Research Institute, University of California, Irvine, California 92697, USA

[a)] **Author to whom correspondence should be addressed:** xiaoqinp@uci.edu

ABSTRACT

In ferroelectric heterostructures, the interaction between intrinsic polarization and the electric field generates a rich set of localized electrical properties. The local electric field is determined by several connected factors, including the charge distribution of individual unit cells, the interfacial electromechanical boundary conditions, and chemical composition of the interfaces. However, especially in ferroelectric perovskites, a complete description of the local electric field across micro-, nano-, and atomic-length scales is missing. Here, by applying four-dimensional scanning transmission electron microscopy (4D STEM) with multiple probe sizes matching the size of structural features, we directly image the electric field of polarization vortices in $(PbTiO_3)_{16}/(SrTiO_3)_{16}$ superlattices and reveal different electric field configurations corresponding to the atomic scale electronic ordering and the nanoscale boundary conditions. The separability of two different fields probed by 4D STEM offers the possibility to reveal how each contributes to the electronic properties of the film.

The electrical properties offered by nanostructured ferroelectric materials make them among top candidates for applications toward next-generation electronic devices.[1–5] In ferroelectrics, the polarization can interact with the boundary conditions of thin films' heterostructures, resulting in various configurations that modify the electric field and charge distribution. Certain polarization patterns can lead to charge accumulation at the domain walls[6–8] and interfaces,[9–12] which could be used for low-power electronic devices. Recently, in ferroelectric multilayers, polarization-vortex structures have been demonstrated to host charge accumulation at their cores[13] and regions of stable negative capacitance.[14] Many exotic states in ferroelectrics are found and studied with the assistance of advanced structural characterization using transmission electron microscopy (TEM). With the latest development of differential-phase contrast (DPC), four-dimensional scanning transmission electron microscopy (4D STEM), and holography in TEM, the electric field and charge in a sample can be resolved at the atomic scale in a S/TEM.[15–19]

4D STEM is a versatile technique due to the flexibility of the experimental setup.[20] However, its complexity also challenges our current understanding and interpretation of the data, as each measurement can be strongly affected by the experimental conditions. In 4D STEM, electrical properties are interrogated through changes in the momentum distribution of a converged electron probe as it passes through the sample.[18] Therefore, the condition of the electron probe is a fundamental part of how it inter-

acts with the sample.[19] For electric-field measurements in STEM, there are generally two classes of electron probes used, which can be defined by their probe size or, equivalently, convergence angle: picometer-sized probes (semi-convergence angle >20 mrad, probe size < 0.8 Å) and nanometer-size probes (semi-convergence angle < 2.5 mrad, probe size >0.5 nm). With a picometer-sized probe, the electric field and charge density surrounding individual atomic columns can be imaged with DPC.[15,16,21] Similarly, 4D STEM has been used to study the electric field and charge densities in 2D materials,[22–24] GaN/AlN nanowires,[25] electride materials,[26] and ferroelectric heterostructures.[10,27] While nanoscale probes have much lower spatial resolution, they also offer larger field of view and greater flexibility in what can be extracted from the 4D STEM data. When the diffraction disks are well separated, the internal electric field can be measured from the center disk while the polarization or strain can be determined from the diffracted disks in the same dataset,[14,28–30] enabling other electronic properties to be determined, such as the permittivity.[14,31]

While 4D STEM/DPC electric-field measurements in ferroelectrics have uncovered several novel phenomena,[10,14,27] the split in the approaches to measuring the electric field has also generated a range of different results that, when considered together, do not always present a consistent picture. Investigations of $BiFeO_3$ (BFO), another perovskite ferroelectric (ABO_3 structure), with a highly convergent probe, have indicated that the electric field is biased along the local polarization direction,[10,27,32] but measurements from the $PbTiO_3$ (PTO) layer in $(PTO)_{12}/(STO)_{12}$ superlattices using a low-convergence probe do not exhibit a similar pattern.[14] How the polarization and built-in electric field in ferroelectric materials interact with the electron probe across all probe sizes and the mechanism for the interaction are still unclear. Here, we present measurements of the electric field using both classes of probes in the same material to understand why differing electric-field patterns have been observed and propose a model to explain them. We have chosen polarization vortex structures in $(PTO)_{16}/(STO)_{16}$ superlattices grown on $DyScO_3$ (110) substrates as a model system, as shown in Fig. 1(a). In a map of the electric field using a picometer-sized probe, we find that it exhibits the same vortex structure as the atomic polarization. In a map measured with a nanometer-sized probe, however, we do not observe the same vortex pattern. Combining this information with phase-field simulations, we show that the coexistence of these two patterns can be attributed to two different mechanisms for generating the electric field.

The electric field in the vortex structures is determined by analyzing changes in the intensity distribution of convergent beam electron diffraction (CBED) patterns as the electron probe raster scans across the sample. As the probe propagates through an electric field, it interacts via the Lorentz force, shifting the probe's momentum. Since the electron diffraction patterns are a momentum space image of the electron probe, by capturing a CBED pattern for every probe position, it is possible to deduce the electric field in the sample.[18,19] This is depicted schematically in Fig. 1(b); see the supplementary material for additional details.

To image the electric field in high resolution, we used a 33-mrad convergence angle, which results in an electron probe with full width at half maximum (FWHM) of 0.6 Å; this is small compared to the (100) lattice spacing of STO and PTO, both close to 4 Å, as illustrated in Fig. 1(c).[4] The 4D STEM data were collected with a 0.3 Å step size, covering three vortices; a survey image with a conventional polarization map from the region, based on titanium/oxygen column displacement, is shown in Fig. 2(a). The projected electric field magnitude is shown in Fig. 2(b). In non-polar materials, the electric

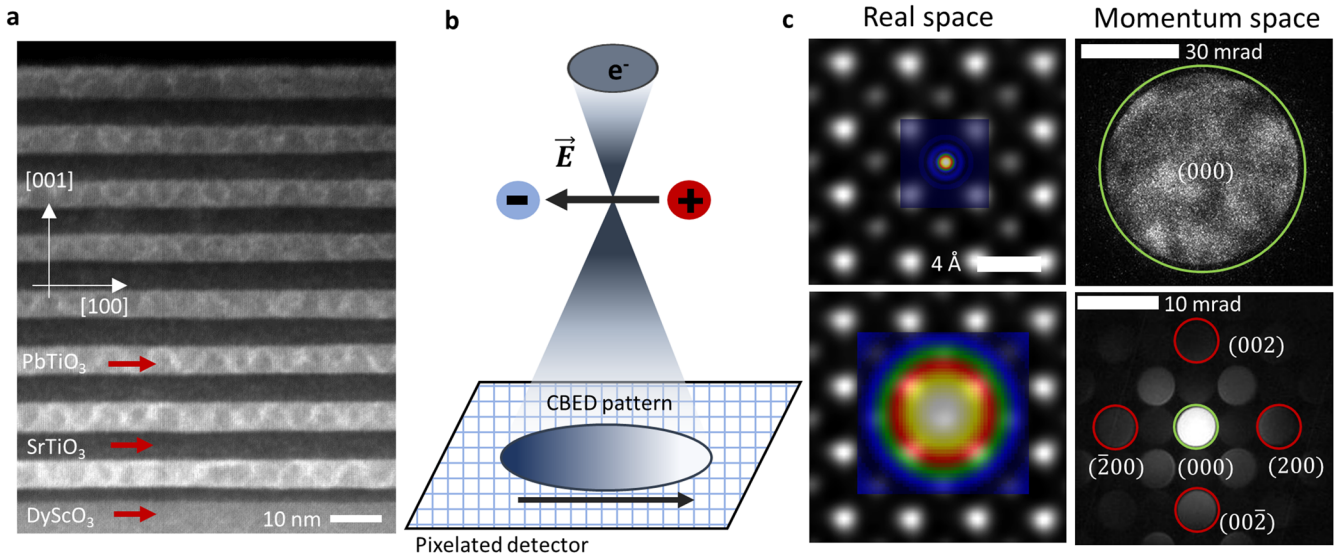

FIG. 1. (a) An ADF image of PTO/STO superlattice. The vortex structures are visible as the contrast variations in the PTO layers. (b), A schematic depiction of the electron probe interacting with an electric field. (c), Left column: the simulated 2D electron probe shapes for 33 mrad (top) and 2.4 mrad (bottom) convergence-angle electron probes overlaid on a HAADF image of STO. Right column: Experimental CBED patterns for the corresponding convergence angles from PTO. The center disks (green) are used to determine the electric field. The diffracted disks (red) in the 2.4 mrad CBED pattern are used to calculate the polarization.

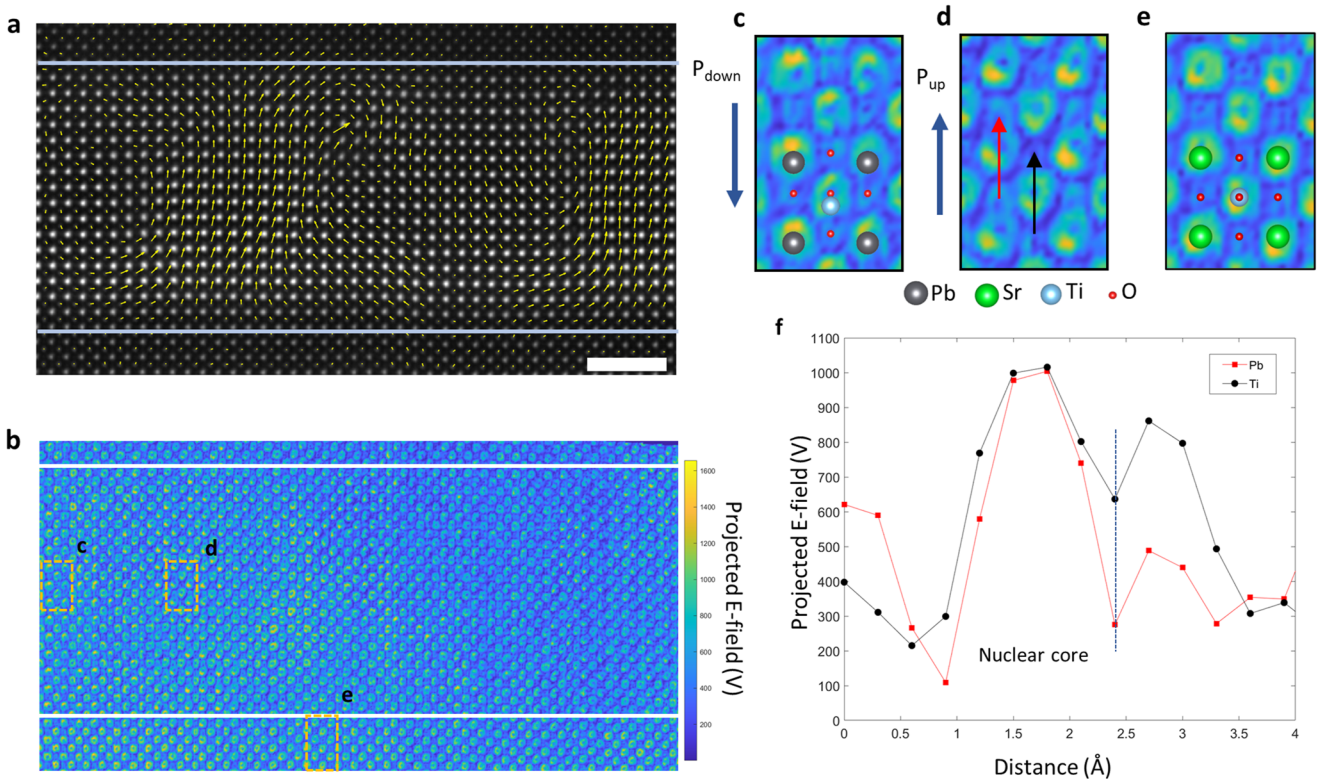

FIG. 2. (a) A HAADF survey image collected simultaneously with 4D STEM data. Atomic displacements are overlaid in yellow. Scale bar is 2 nm. (b) Electric field mapping of the same region in (a). (c) Zoomed-in view of a region with polarization down. (d) A zoomed-in view with polarization up. Red and black arrows indicate the position of the line profiles across lead and titanium/oxygen columns, respectively, as shown in (f). (e) A zoomed-in view of the highlighted region in STO. (f) Line profiles of the electric field magnitude across lead and titanium/oxygen columns.

field surrounding each atomic column points radially outward and is mostly rotationally symmetric, as can be observed in the STO layers near the top and bottom of Fig. 2(b). However, the electric field of cation columns in PTO shows a strong asymmetry, depending on the polarization direction. Figs. 2(c)–2(e) show detailed views of the electric field in regions with polarization down and up in PTO and a region with no polarization in STO, respectively. The electric-field bias in Figs. 2(c) and 2(d) points opposite to the local polarization measured by the atomic displacement in Fig. 2(a). Line profiles from regions marked in Fig. 2(d) of the electric field magnitude illustrate this quantitatively, as shown in Fig. 2(f) for both, lead (red) and titanium/oxygen (black) columns, in a region with polarization up. The projected electric field on the bottom side of both lead and titanium/oxygen columns peaks at over 1 kV. On the top side of the column, the electric field of the lead column peaks at 488.3 V, while that of the titanium/oxygen column peaks at 861.3 V. These line profiles are indicative of a general trend, where lead columns exhibit a strongly asymmetric electric field, while titanium/oxygen columns exhibit weaker asymmetry. Some titanium/oxygen columns even appear almost perfectly symmetric, as shown in Fig. S1.

To further analyze the electric-field distribution surrounding each atomic column, we segmented a region of radius 0.9 Å surrounding each A-site (lead or strontium) column and calculated the average electric-field vector within this region. With this method, atomic columns with a strong asymmetry will have a large average electric field, while columns with a more symmetric field distribution will have a small average field. This is applied to the full dataset in Fig. 3(a), where vectors of the average electric field of the A-site columns are overlaid on the full electric field map. Detailed views for the same regions highlighted in Figs. 2(c)–2(e) are shown in Figs. 3(b)–3(d), respectively. Figure 3(e) shows the average electric field overlaid on a HAADF image for clarity. Examining the entire region, we can see that the average electric field of each A-site column follows a vortex pattern that is coincident with that shown in the conventional polarization map [Fig. 2(b)]. Notably, this vortex pattern is unique to the lead sites in the PTO lattice. While some titanium/oxygen columns do show an electric field bias, repeating this same analysis for the whole dataset does not show significant ordering in the electric field (see Fig. S3). Averaging the electric field over each unit cell also does not reveal the same vortex pattern (see Fig. S4).

The dominant nature of the A-site electric field and correlation with the structural polarization in PTO agrees with previous studies of the atomic-scale electric field in BFO.[10,27] Interestingly, in both materials, first principles calculations have shown that the 6s electrons of both lead and bismuth form covalent bonds when

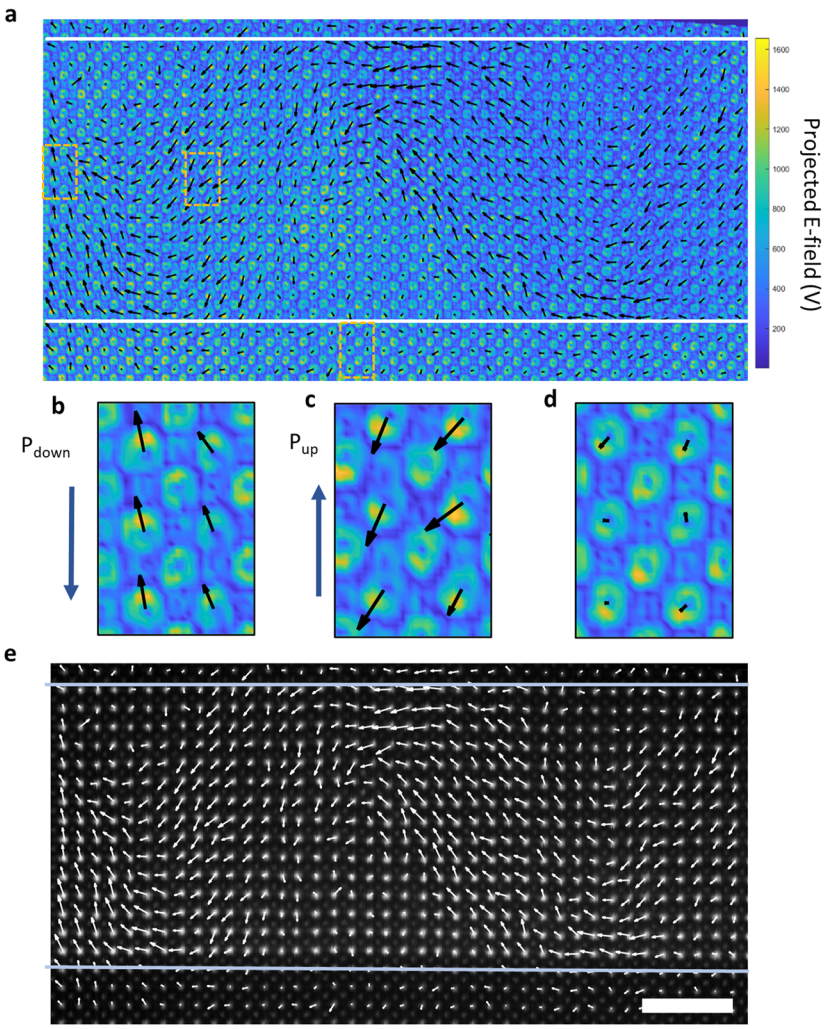

FIG. 3. (a), The high-convergence angle, electric field map with a vector map of the average lead column electric field overlaid in black. (b)–(d) Zoomed-in views of the electric field from the highlighted regions [same regions as Figs. 2(c)–2(e)]. (e) The vector map of the average Pb column electric field, overlaid on a reconstructed HAADF image; the arrow color is changed to white to aid visibility. Scale bar is 2 nm.

they hybridize with the oxygen 2p electrons.[33–35] The 6s lone-pair forms a localized lobe that pushes the A-site cation away from the center of the unit cell, causing cooperative displacement of B-site cations and the oxygen octahedron. The combined off-center position of the 6s lone pair and the associated lattice distortion results in the polarization of the unit cell. This indicates that the electric field bias surrounding lead atomic columns observed here and on the bismuth columns in previous studies may have a common origin in the covalent bond between the A-site and oxygen atoms.[10] It also provides an explanation for why the same electric field bias is not consistently observed on titanium/oxygen columns. Although titanium 3d orbitals also hybridize with oxygen 2p, the hybridization is not driven by a localized lone pair. First principles calculations have shown weaker charge separation near B-site columns compared to A-site columns, which would make the electric field asymmetry weaker compared to A-site columns.[34] Similar studies of 2D materials have also shown that 4D STEM is highly sensitive to bonding structure, which can be revealed by changes in the electric field or charge density.[22–24,36]

To study the electric field at the nanometer scale, we formed an electron probe with a 2.4- mrad semi-convergence angle, resulting in a probe FWHM of 4 Å, close to the (100) lattice spacing in both STO and PTO [Fig. 1(c)]. In this beam condition, the diffraction disks are well separated. 4D STEM data were collected in this beam condition with a 1.5 Å step size; a virtual bright-field image of a PTO layer from this dataset is shown in Fig. 4(a). The polarization of the PTO layer can be measured directly in this beam condition, based on changes in the symmetry of the intensity distribution in conjugate pair diffraction disks in each diffraction pattern[14,28] (for further information, see the supplementary material). The polarization in this region is mapped in Fig. 4(b) and exhibits the characteristic vortex pattern. We measured the electric field only from the momentum change of the center disk to exclude any effects due to polarization or strain that may shift the diffraction disks. A map of the electric field in-plane and out-of-plane components (E_x, E_y) in this region is shown in Figs. 4(c) and 4(d), respectively; a Gaussian blur is applied to reduce noise. With a maximum value of nearly 10 V inside the PTO layer, the projected electric field measured in this condition

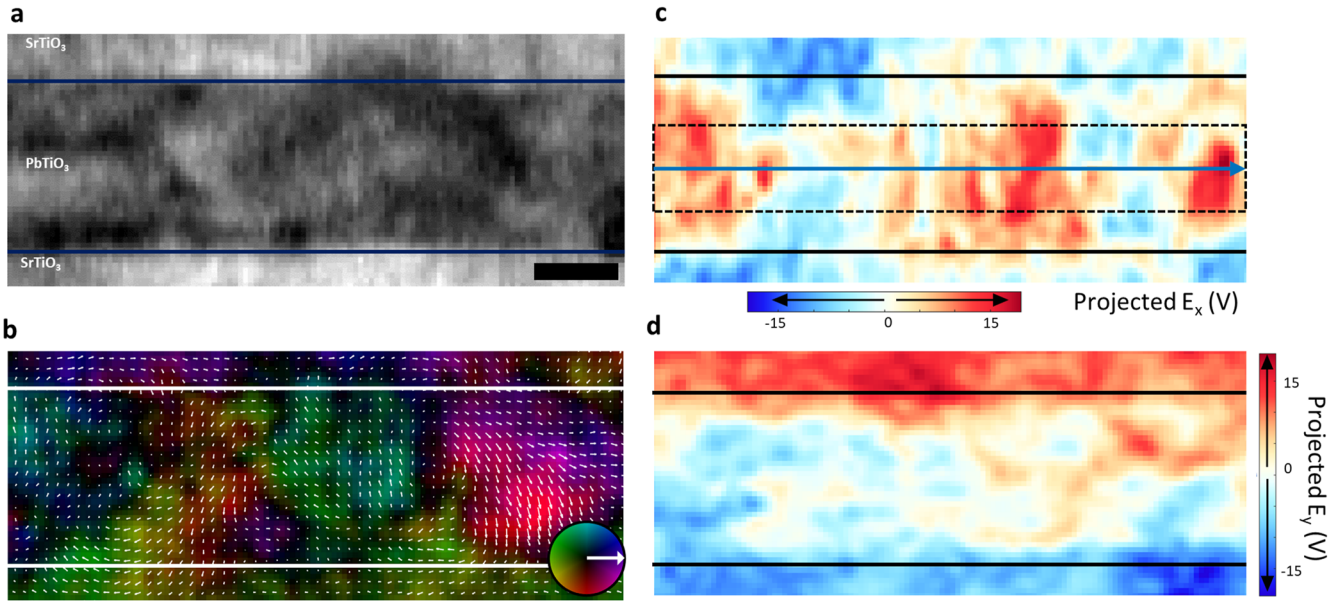

FIG. 4. (a) A bright-field image reconstructed from the 4D STEM data. (b) The polarization mapping from the same dataset shows that this region covers three vortices. (c) and (d) The x-component (c) and the y-component (d) of the projected electric field, measured from the (000) disk. The dashed box and arrow shows the position of a line profile shown in Fig. 5(d). The scale bar on (a) is 3 nm.

is much weaker than the field measured with the picometer probe, and it also does not show the same vortex pattern as before. Instead, the electric field is separated into regions that are mostly oriented in-plane (E_x), along [100] or [$\bar{1}$00], in the middle of the PTO layer. Ordering in the out-of-plane component (E_y) is less clear. The electric field at the edge of the PTO and in the adjacent STO layers is not reliable due to a shift in zone-axis alignment between adjacent layers of the superlattice, which affects the intensity distribution in the CBED pattern. We also measured the polarization using conventional displacement mapping from a nearby region, which also showed polarization-vortex structures (see Fig. S5).

We also performed phase-field simulations of the polarization and electric field in the $(PTO)_{16}/(STO)_{16}$ superlattice. The polarization and electric field components are shown in Figs. 5(a)–5(c). Comparing the electric field from experiment and simulation, the alternating in-plane alignment in the experimental electric field is visible near the center of the simulated electric-field map. The out-of-plane electric field component visible at the edges of the PTO layer in the phase-field simulation is likely not visible in the experiment due to the signal being overshadowed by the shift in the zone-axis between superlattice layers. Line profiles from the marked regions in Figs. 4(e) and 5(c) are shown in Fig. 5(d) for comparison. From the line profile, the alternating field pattern is clear in both experiment and simulation. There is a slight difference in the periodicity of the in-plane components from experiment and simulation, which is also reflected in the polarization map; the width of the polarization-vortex structures is measured to be ~5.5 nm in experiment and 6 nm in simulation (see Fig. S6 for details). Taken together, the electric field and polarization measured with the nanoscale probe both match more closely with results from phase-field simulations. This indicates that the electric field measured with a larger probe size follows the strain and electrical boundary conditions determined by the superlattice structure, as it is in phase-field simulations, and is more representative of the total electric field in the sample. This is also in agreement with previous publications that report the electric field distributions in the $(PTO)_{12}/(STO)_{12}$ superlattice under similar beam conditions.[14]

These differences observed when switching between the picometer and nanometer electron probes are due to changes in the interaction volume in the sample. Variations in the electric field that occur over length scales much smaller than the width of the probe will sum together incoherently and, thus, do not generate a change in probe momentum. For the nanometer-sized probe, the electric-field bias of atomic columns is not detectable, since the probe covers several atomic columns at a time, many with a field that is almost rotationally symmetric. Therefore, only long-range effects that influence the electric field in the entire film are detected with the nanometersized probe. For the picometer-sized probe, the electric-field bias of individual atomic columns, induced by the hybridization of lead 6s, lone-pair electrons, is detectable because of its smaller width and interaction volume. This effect is much stronger in comparison to the total electric field and will dominate the overall pattern, drowning out any effect from the total electric field. Interestingly, when the electric field measured with a picometer-sized probe is averaged over a whole unit cell, it does not match the result from the nanometer probe [compare Figs. 4(b) and S4], even though the FWHM of the probe used to measure the field in Fig. 4(b) is roughly equal to the width of one unit cell. Therefore, even when integrating the signal from the picometer probe over an area roughly equal to that of a nanometer probe, they are not equivalent.

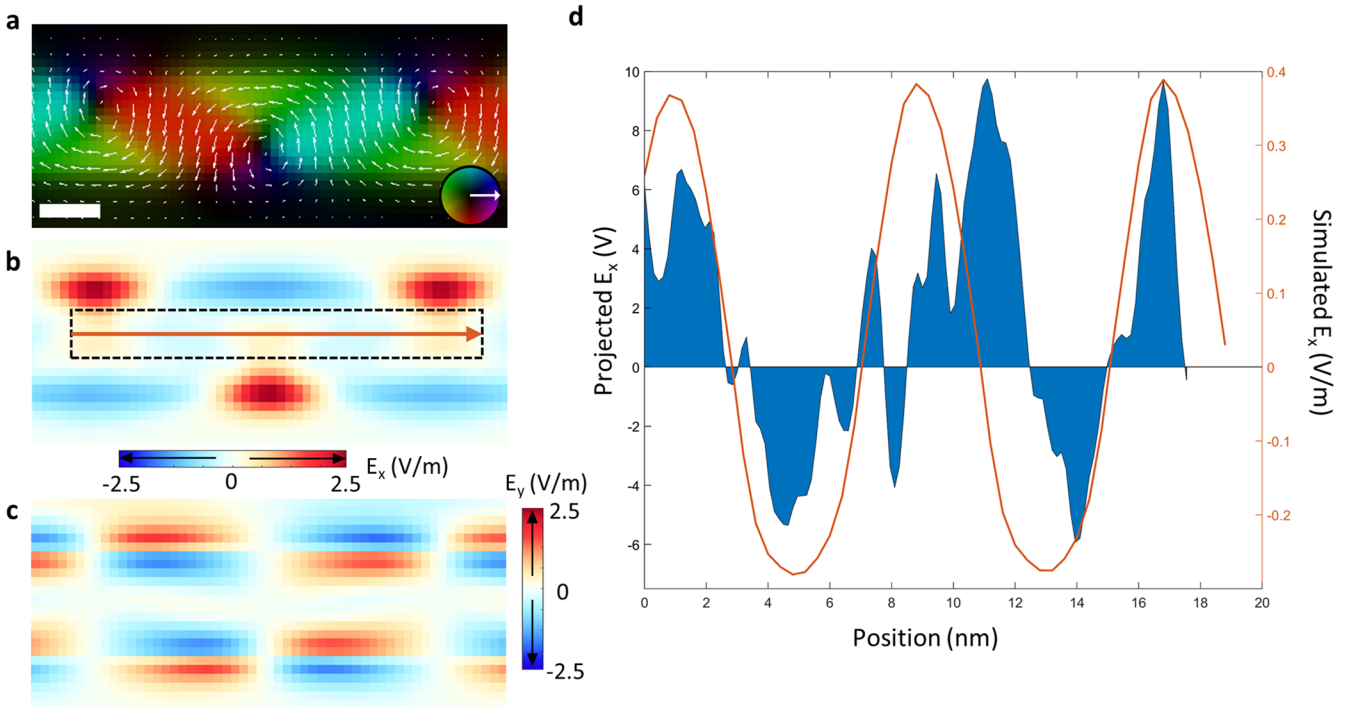

FIG. 5. (a), Polarization of the PTO layer from phase-field simulation. (b) and (c) The electric field components, E_x (b) and E_y (c), from phase-field simulation. (d) Line profiles of the E_x component from experiment (blue) and phase-field simulation (orange) for comparison. Scale bar is 3 nm.

Although we have discussed the differences mainly in terms of probe width, this divergence between the average over the unit cell and over atomic columns indicates that other factors, such as the depth of focus, channeling, and beam broadening, may affect the interaction as well. For on-column probe positions, previous studies of probe channeling have demonstrated that the probe intensity remains on the same atomic column for samples less than 30 nm thick; beyond this, the intensity may jump to a different column. For off-column positions, de-channeling can occur for much thinner samples.[37] For our sample, we measured the thickness of the sample in the region of the high-convergence and low-convergence datasets to be 12 and 16 nm, respectively (see the supplementary material for details), so, de-channeling effects from on-column scan positions should be minimal. However, the de-channeling of off-column scan positions introduces additional noise when integrating over the unit cell, which is likely why the E-field averaged over each unit cell does not reflect the same pattern. Probe broadening can also introduce artifacts in the final E-field, which may depend on the position of the probe and the convergence angle.[19,38] For high convergence angles, it has been shown that proper adjustment of the probe focus position can mitigate the effects of probe broadening and maintain the qualitative accuracy expected for samples in the 5–20 nm thickness range.[38–40]

In summary, we have applied 4D STEM electric field imaging to a $(PTO)_{16}/(STO)_{16}$ superlattice with both a picometer-sized and a nanometer-sized electron probes, and observed different patterns in the electric field at atomic and nanometer scales. The electric field measured by a picometer-sized probe shows a vortex pattern and is mainly determined by the asymmetry introduced to lead atomic columns by the bonding configuration of lead 6s, lone-pair electrons, which generates a dipole in each unit cell. On the other hand, the electric field measured with a nanometer-sized probe follows the total electric field set by the electrostatic and elastic boundary conditions of the film. These differing configurations are caused by a change in the interaction volume of the probe, which causes the dominant contribution to the electric field image to shift from the dipole of individual unit cells to the total electric field in the material when the probe size increases. These findings highlight the versatility of 4D STEM in studying both the bonding structure and electrostatic properties of ferroelectric materials, and elucidates the mechanisms that cause the differing electric field configurations observed in previous studies.

See the supplementary material for details of the film growth, STEM and 4D STEM experiments and data analyses, and phase-field simulations, as well as additional supporting figures.

Microscopy experiments, data analysis, and specimen preparation were supported by the U.S. Department of Energy (DOE), Office of Basic Energy Sciences, Division of Materials and Engineering, under Grant No. DE-SC0014430. Computations for this research were performed on the Pennsylvania State University's

Institute for Computational and Data Sciences' Advanced Cyber-Infrastructure (ICDS-ACI). This work also used the Extreme Science and Engineering Discovery Environment (XSEDE), which is supported by National Science Foundation, under Grant No. ACI-1548562. This work used the Extreme Science and Engineering Discovery Environment (XSEDE) Comet at San Diego State Supercomputing through allocation Grant No. TG-DMR1700006.[41] J.A.Z. and L.Q.C. are supported by the Computational Materials Sciences Program , funded by the U.S. Department of Energy, Office of Science, Basic Energy Sciences, under Award No. DE-SC0020145 (Program Manager: Matthias Graf Matthias.Graf@science.doe.gov). J.A.Z. would also like to acknowledge support from 3M Incorporated in the form of a fellowship. L.W.M. acknowledges support from the U.S. Department of Energy, Office of Science, Office of Basic Energy Sciences, under Award No. DE-SC-0012375, for the development of ferroic thin films. S.D. and R.R. acknowledge support through the Quantum Materials program, funded by the U.S. Department of Energy, Office of Science, Basic Energy Sciences, Materials Sciences and Engineering Division. STEM experiments were conducted using the facilities in the Irvine Materials Research Institute (IMRI) at the University of California, Irvine. The authors would like to thank Toshihiro Aoki of IMRI for his help during STEM experiments.

AUTHOR DECLARATIONS

Conflict of Interest

The authors have no conflicts to disclose.

Author Contributions

X.Q.P. concieved and directed this project. C.A. and W.G. conducted STEM and 4D-STEM characterization and data analysis. J.G. and L.Z. also performed analysis of 4D-STEM data. C.Q. prepared TEM lamella. J.A.Z. performed phase-field simulations under supervision of L.Q.C. S.D. synthesized the superlattice films under supervision of L.W.M. and R.R. C.A., W.G., and X.Q.P. prepared the manuscript with discussion and contributions from all co-authors.

Christopher Addiego: Data curation (lead); Formal analysis (lead); Investigation (lead); Methodology (lead); Software (lead); Validation (lead); Visualization (lead); Writing – original draft (lead); Writing – review & editing (lead). **Jacob A. Zorn**: Data curation (equal); Formal analysis (equal); Methodology (equal); Software (equal); Visualization (equal). **Wenpei Gao**: Data curation (equal); Formal analysis (equal); Investigation (equal); Writing – original draft (equal); Writing – review & editing (equal). **Sujit Das**: Methodology (equal). **Jiaqi Guo**: Methodology (supporting). **Chengqing Qu**: Methodology (supporting). **Liming Zhao**: Methodology (supporting). **Lane W. Martin**: Conceptualization (supporting); Funding acquisition (supporting); Supervision (supporting). **Ramamoorthy Ramesh**: Conceptualization (supporting); Funding acquisition (supporting); Supervision (supporting). **Long-Qing Chen**: Conceptualization (supporting); Funding acquisition (supporting); Supervision (supporting). **Xiaoqing Pan**: Conceptualization (lead); Data curation (equal); Formal analysis (equal); Funding acquisition (equal); Supervision (lead); Writing – original draft (equal); Writing – review & editing (equal).

DATA AVAILABILITY

The data that support the findings of this study are available from the corresponding author upon reasonable request.

REFERENCES

[1] S.-T. Han, Y. Zhou, and V. A. L. Roy, Adv. Mater. **25**, 5425 (2013).
[2] D. S. Jeong, R. Thomas, R. S. Katiyar, J. F. Scott, H. Kohlstedt, A. Petraru, and C. S. Hwang, Rep. Prog. Phys. **75**, 076502 (2012).
[3] R. Ramesh and D. G. Schlom, Nat. Rev. Mater. **4**, 257 (2019).
[4] D. G. Schlom, L.-Q. Chen, C.-B. Eom, K. M. Rabe, S. K. Streiffer, and J.-M. Triscone, Annu. Rev. Mater. Res. **37**, 589 (2007).
[5] J. F. Scott, Jpn. J. Appl. Phys. **38**, 2272 (1999).
[6] Y. Zhang, H. Lu, X. Yan, X. Cheng, L. Xie, T. Aoki, L. Li, C. Heikes, S. P. Lau, D. G. Schlom, L. Chen, A. Gruverman, and X. Pan, Adv. Mater. **31**, 1902099 (2019).
[7] L. Li, J. Britson, J. R. Jokisaari, Y. Zhang, C. Adamo, A. Melville, D. G. Schlom, L.-Q. Chen, and X. Pan, Adv. Mater. **28**, 6574 (2016).
[8] J. Ma, J. Ma, Q. Zhang, R. Peng, J. Wang, C. Liu, M. Wang, N. Li, M. Chen, X. Cheng, P. Gao, L. Gu, L.-Q. Chen, P. Yu, J. Zhang, and C.-W. Nan, Nat. Nanotechnol. **13**, 947 (2018).
[9] Y. Zhang, L. Xie, J. Kim, A. Stern, H. Wang, K. Zhang, X. Yan, L. Li, H. Liu, G. Zhao, H. Chi, C. Gadre, Q. Lin, Y. Zhou, C. Uher, T. Chen, Y.-H. Chu, J. Xia, R. Wu, and X. Pan, Nat. Commun. **9**, 685 (2018).
[10] W. Gao, C. Addiego, H. Wang, X. Yan, Y. Hou, D. Ji, C. Heikes, Y. Zhang, L. Li, H. Huyan, T. Blum, T. Aoki, Y. Nie, D. G. Schlom, R. Wu, and X. Pan, Nature **575**, 480 (2019).
[11] Y. Zhang, H. Lu, L. Xie, X. Yan, T. R. Paudel, J. Kim, X. Cheng, H. Wang, C. Heikes, L. Li, M. Xu, D. G. Schlom, L.-Q. Chen, R. Wu, E. Y. Tsymbal, A. Gruverman, and X. Pan, Nat. Nanotechnol. **13**, 1132 (2018).
[12] C. Chen, S. Lv, J. Li, Z. Wang, X. Liang, Y. Li, D. Viehland, K. Nakajima, and Y. Ikuhara, Appl. Phys. Lett. **107**, 031601 (2015).
[13] K. Du, M. Zhang, C. Dai, Z. N. Zhou, Y. W. Xie, Z. H. Ren, H. Tian, L. Q. Chen, G. Van Tendeloo, and Z. Zhang, Nat. Commun. **10**, 4864 (2019).
[14] A. K. Yadav, K. X. Nguyen, Z. Hong, P. García-Fernández, P. Aguado-Puente, C. T. Nelson, S. Das, B. Prasad, D. Kwon, S. Cheema, A. I. Khan, C. Hu, J. Íñiguez, J. Junquera, L.-Q. Chen, D. A. Muller, R. Ramesh, and S. Salahuddin, Nature **565**, 468 (2019).
[15] N. Shibata, S. D. Findlay, Y. Kohno, H. Sawada, Y. Kondo, and Y. Ikuhara, Nat. Phys. **8**, 611 (2012).
[16] N. Shibata, T. Seki, G. Sánchez-Santolino, S. D. Findlay, Y. Kohno, T. Matsumoto, R. Ishikawa, and Y. Ikuhara, Nat. Commun. **8**, 15631 (2017).
[17] N. Shibata, S. D. Findlay, T. Matsumoto, Y. Kohno, T. Seki, G. Sánchez-Santolino, and Y. Ikuhara, Acc. Chem. Res. **50**, 1502 (2017).
[18] K. Müller, F. F. Krause, A. Béché, M. Schowalter, V. Galioit, S. Löffler, J. Verbeeck, J. Zweck, P. Schattschneider, and A. Rosenauer, Nat. Commun. **5**, 5653 (2014).
[19] K. Müller-Caspary, F. F. Krause, T. Grieb, S. Löffler, M. Schowalter, A. Béché, V. Galioit, D. Marquardt, J. Zweck, P. Schattschneider, J. Verbeeck, and A. Rosenauer, Ultramicroscopy **178**, 62 (2017).
[20] C. Ophus, Microsc. Microanal. **25**(3), 563 (2019).
[21] G. Sánchez-Santolino, N. R. Lugg, T. Seki, R. Ishikawa, S. D. Findlay, Y. Kohno, Y. Kanitani, S. Tanaka, S. Tomiya, Y. Ikuhara, and N. Shibata, ACS Nano **12**(9), 8875 (2018).
[22] S. Fang, Y. Wen, C. S. Allen, C. Ophus, G. G. D. Han, A. I. Kirkland, E. Kaxiras, and J. H. Warner, Nat. Commun. **10**, 1127 (2019).

[23]K. Müller-Caspary, M. Duchamp, M. Rösner, V. Migunov, F. Winkler, H. Yang, M. Huth, R. Ritz, M. Simson, S. Ihle, H. Soltau, T. Wehling, R. E. Dunin-Borkowski, S. Van Aert, and A. Rosenauer, Phys. Rev. B **98**, 121408 (2018).
[24]R. Ishikawa, S. D. Findlay, T. Seki, G. Sánchez-Santolino, Y. Kohno, Y. Ikuhara, and N. Shibata, Nat. Commun. **9**, 3878 (2018).
[25]K. Müller-Caspary, T. Grieb, J. Müßener, N. Gauquelin, P. Hille, J. Schörmann, J. Verbeeck, S. Van Aert, M. Eickhoff, and A. Rosenauer, Phys. Rev. Lett. **122**, 106102 (2019).
[26]Q. Zheng, T. Feng, J. A. Hachtel, R. Ishikawa, Y. Cheng, L. Daemen, J. Xing, J. C. Idrobo, J. Yan, N. Shibata, Y. Ikuhara, B. C. Sales, S. T. Pantelides, and M. Chi, Sci. Adv. **7**, eabe6819 (2021).
[27]M. Campanini, R. Erni, C. H. Yang, R. Ramesh, M. D. Rossell, C. H. Yang, R. Ramesh, and M. D. Rossell, Nano Lett. **18**, 717 (2018).
[28]K. Tsuda, A. Yasuhara, and M. Tanaka, Appl. Phys. Lett. **103**, 082908 (2013).
[29]D. Carvalho, K. Müller-Caspary, M. Schowalter, T. Grieb, T. Mehrtens, A. Rosenauer, T. Ben, R. García, A. Redondo-Cubero, K. Lorenz, B. Daudin, and F. M. Morales, Sci. Rep. **6**, 28459 (2016).
[30]V. B. Ozdol, C. Gammer, X. G. Jin, P. Ercius, C. Ophus, J. Ciston, and A. M. Minor, Appl. Phys. Lett. **106**, 253107 (2015).
[31]S. Das, Z. Hong, V. A. Stoica, M. A. P. Gonçalves, Y. T. Shao, E. Parsonnet, E. J. Marksz, S. Saremi, M. R. McCarter, A. Reynoso, C. J. Long, A. M. Hagerstrom, D. Meyers, V. Ravi, B. Prasad, H. Zhou, Z. Zhang, H. Wen, F. Gómez-Ortiz, P. García-Fernández, J. Bokor, J. Íñiguez, J. W. Freeland, N. D. Orloff, J. Junquera, L. Q. Chen, S. Salahuddin, D. A. Muller, L. W. Martin, and R. Ramesh, Nat. Mater. **20**, 194 (2021).
[32]H. Huyan, L. Li, C. Addiego, W. Gao, and X. Pan, Natl. Sci. Rev. **6**, 669 (2019).
[33]R. E. Cohen, Nature **358**, 136 (1992).
[34]P. Ravindran, R. Vidya, A. Kjekshus, H. Fjellvåg, and O. Eriksson, Phys. Rev. B **74**, 224412 (2006).
[35]K. C. Pitike, W. D. Parker, L. Louis, and S. M. Nakhmanson, Phys. Rev. B **91**, 035112 (2015).
[36]Y. Wen, S. Fang, M. Coupin, Y. Lu, C. Ophus, E. Kaxiras, and J. H. Warner, ACS Nano **16**, 6657 (2022).
[37]P. M. Voyles, J. L. Grazul, and D. A. Muller, Ultramicroscopy **96**, 251 (2003).
[38]C. Addiego, W. Gao, and X. Pan, Ultramicroscopy **208**, 112850 (2020).
[39]J. Bürger, T. Riedl, and J. K. N. Lindner, Ultramicroscopy **219**, 113118 (2020).
[40]H. L. Robert, I. Lobato, F. J. Lyu, Q. Chen, S. Van Aert, D. Van Dyck, and K. Müller-Caspary, Ultramicroscopy **233**, 113425 (2022).
[41]J. Towns, T. Cockerill, M. Dahan, K. Gaither, A. Grimshaw, V. Hazlewood, S. Lathrop, D. Lifka, G. D. Peterson, R. Roskies, J. R. Scott, and N. Wilkens-Diehr, Computing in Science and Engineering **16**(5), 62 (2014).